nature climate change

Article

https://doi.org/10.1038/s41558-026-02712-y

Particulate air pollution undermines plant water-use efficiency by inhibiting photosynthesis

Received: 5 November 2025

Accepted: 24 June 2026

Published online: 17 August 2026

Check for updates

Jian Wang[1,2,3], Yuyu Zhou[1,4] ✉, Lingli Liu[3,5,6], Constantin M. Zohner[7,8], Jing Wei[9] & Chaoyang Wu[2,3] ✉

Rising atmospheric CO_2 and climate change have generally enhanced plant water-use efficiency (WUE), yet the influence of fine particulate pollution ($PM_{2.5}$) on this carbon–water coupling remains poorly understood. Drawing on a global database of tree-ring isotopes, eddy-covariance fluxes and satellite-derived vegetation metrics, here we show that $PM_{2.5}$ exerts a predominantly negative influence on WUE across spatial scales. The magnitude of this effect varies geographically and is modulated by interactions among vegetation traits, pollution levels and climate, with forests and non-forests exhibiting distinct patterns. The WUE decline arises primarily from the $PM_{2.5}$-induced suppression of photosynthesis rather than changes in evapotranspiration, due to reduced photosynthetically active radiation and carboxylation capacity. Current ecosystem models that omit aerosol processes fail to reproduce the observed $PM_{2.5}$–WUE relation, which indicates that covarying climate drivers alone are insufficient to explain this effect. Our findings identify $PM_{2.5}$ as an overlooked yet critical factor that weakens plant carbon–water coupling under climate change.

Terrestrial carbon and water cycles are tightly coupled through gas exchange regulated by plant stomata[1,2]. Plant water-use efficiency (WUE), defined as the ratio of carbon assimilation to water loss, serves as an integrative indicator of plant resilience and acclimation strategies under environmental stress, as it links carbon uptake with water consumption from the leaf to the ecosystem level[1,3,4]. Elevated atmospheric CO_2 is widely recognized as a primary driver of increasing WUE, a phenomenon known as the CO_2 fertilization effect[5–8]. At the leaf level, increases in intrinsic WUE (iWUE; the instantaneous ratio between C assimilation rate and stomatal conductance) are largely attributed to CO_2-enhanced photosynthesis and reduced stomatal conductance[9,10]. At the ecosystem scale, higher CO_2 can boost gross primary productivity (GPP) while potentially reducing evapotranspiration (ET), thereby increasing ecosystem WUE (WUE_{eco}; the ratio of GPP and ET)[4,11]. Less well understood, but potentially important, is the role of air pollution, which may offset the expected CO_2-driven gains in WUE. Although global concentrations of fine particulate matter ($PM_{2.5}$) have declined in recent years, it remains widespread across large regions due to continuing urbanization and increasing wildfire activity[12]. Despite its prevalence, the effects of $PM_{2.5}$ on plant functioning, acclimation and carbon–water coupling have received limited attention.

[1]Department of Geography, The University of Hong Kong, Hong Kong, China. [2]The Key Laboratory of Land Surface Pattern and Simulation, Institute of Geographical Sciences and Natural Resources Research, Chinese Academy of Sciences, Beijing, China. [3]University of the Chinese Academy of Sciences, Beijing, China. [4]Institute for Climate and Carbon Neutrality, The University of Hong Kong, Hong Kong, China. [5]State Key Laboratory of Vegetation and Environmental Change, Institute of Botany, Chinese Academy of Sciences, Beijing, China. [6]China National Botanical Garden, Beijing, China. [7]Institute for Future Initiatives, The University of Tokyo, Tokyo, Japan. [8]BRANCH Institute, Zug, Switzerland. [9]MEEKL-AERM, College of Environmental Sciences and Engineering, Institute of Tibetan Plateau, and Center for Environment and Health, Peking University, Beijing, China. ✉e-mail: yuyuzhou@hku.hk; wucy@igsnrr.ac.cn

Although the roles of CO_2, climatic factors, vegetation traits and soil nutrient status in regulating carbon and water fluxes are well established[4,8,13–18], the global impacts of recent changes in $PM_{2.5}$ concentrations on plant WUE remain poorly understood. In heavily polluted environments, including urban centres and fire-prone regions, $PM_{2.5}$ particles can accumulate on leaf surfaces and within stomatal pores, where they physically block gas exchange pathways[19]. This interference can reduce both stomatal conductance and net photosynthesis, with the net effect on WUE depending on which process is more strongly affected[20]. $PM_{2.5}$ also alters the light environment by modifying the balance between direct and diffuse radiation[21], leading to complex and sometimes opposing effects on WUE. On one hand, elevated aerosol loads can limit photosynthetically active radiation (PAR)[22], thereby suppressing carbon uptake and potentially decreasing WUE. On the other hand, increases in diffuse radiation may enhance photosynthesis in shaded leaves more than they increase transpiration[23], thereby improving WUE. The effects of $PM_{2.5}$ may further depend on its source. Fire-derived aerosols can alleviate nutrient limitations, such as nitrogen and phosphorus, through deposition[24], thereby potentially enhancing carbon assimilation and WUE in nutrient-poor ecosystems. By contrast, $PM_{2.5}$ from urban and industrial sources often contains heavy metals and polycyclic aromatic hydrocarbons that can penetrate leaf tissues, induce oxidative stress and impair photosynthesis[25], further diminishing WUE.

Empirical evidence from manipulative experiments, site-level monitoring and satellite observations has yielded inconsistent findings on the $PM_{2.5}$–WUE relation[19,20,26], probably due to differences in WUE proxies, ecological context or methodological approaches. These discrepancies hinder the identification of generalizable patterns and underlying mechanisms. To address this gap, we synthesized a broad suite of WUE proxies, including tree-ring isotopic discrimination for 73 species (Supplementary Table 1), eddy-covariance flux measurements (Supplementary Table 2) and an ensemble of satellite-based estimates, to systematically evaluate plant WUE responses to $PM_{2.5}$ pollution. We applied spatial attribution analyses to assess the heterogeneity of the $PM_{2.5}$–WUE relation for forests and non-forests. We further explored potential regulatory mechanisms underpinning $PM_{2.5}$ effects using a casual detection framework. Finally, we examined climate-only explanations for $PM_{2.5}$ effects using 15 state-of-the-art terrestrial ecosystem models (Supplementary Table 3).

Inhibitive effects of $PM_{2.5}$ pollution on plant WUE

We analysed tree-ring-based iWUE and flux-based WUE_{eco} across angiosperm and gymnosperm species and plant functional types (Supplementary Fig. 1). Site–year combined anomalies of iWUE were negatively associated with anomalies of $PM_{2.5}$ ($r = -0.15$, $P < 0.001$), with a stronger negative association for angiosperms ($r = -0.28$, $P < 0.001$) than for gymnosperms ($r = -0.04$, $P = 0.298$) (Fig. 1a). After accounting for multicollinearity between $PM_{2.5}$ and potential covarying drivers, a ridge regression analysis confirmed a negative $PM_{2.5}$ sensitivity ($SV_{PM2.5}$) for iWUE. The covariates were CO_2, climate (vapor pressure deficit (VPD), temperature (TMP), precipitation (PPT) and shortwave radiation (RAD)) and ozone (O_3). Across 27 tree species with at least 10 site–year records, 21 showed negative $SV_{PM2.5}$ (nine significant), whereas six exhibited positive $SV_{PM2.5}$ (two significant, $P < 0.05$; Supplementary Fig. 2). Flux-based WUE_{eco} also showed a negative relation with $PM_{2.5}$ ($r = -0.21$, $P < 0.001$), with a stronger correlation in forests ($r = -0.22$, $P < 0.001$) than in non-forests ($r = -0.19$, $P < 0.001$), consistent with the ridge regression results (Fig. 1b). Predominantly negative $SV_{PM2.5}$ for flux-based WUE_{eco} was also detected in a vegetation-specific analysis (Supplementary Fig. 3) and a site-specific analysis (Supplementary Fig. 4).

A regression analysis using an ensemble of satellite-based WUE_{eco} estimates revealed predominantly negative $PM_{2.5}$ effects, with 62.5% of grids showing negative $SV_{PM2.5}$ (24.4% significant, $P < 0.05$) and 37.5% showing positive $SV_{PM2.5}$ (13.2% significant) (Fig. 1c). Grouping grid cells into vegetation types confirmed the inhibitive effects of $PM_{2.5}$ across plant functional types, with stronger effects in forests than in non-forests (Fig. 1d). Across environmental drivers, CO_2 and TMP showed overall positive impacts on satellite-based WUE_{eco}, whereas the negative effect of $PM_{2.5}$ was comparable in magnitude with those of VPD and PPT (Fig. 1e). Using generalized additive models to partition the interannual variance in WUE, we found that CO_2, TMP and VPD remained the dominant controls on WUE variability, as they collectively explain more than half of the total variance. Importantly, $PM_{2.5}$ alone explains on average 12.7 ± 0.3% of the WUE variance (Supplementary Fig. 5).

Biome-dependent spatial heterogeneity of $PM_{2.5}$ effects

Using an extreme gradient boosting (XGBoost) model combined with a Shapley additive explanations (SHAP) analysis (Methods), we quantified the spatial attribution of $PM_{2.5}$ effects on WUE, represented by satellite-based $SV_{PM2.5}$, for forests and non-forests. The model predicted $SV_{PM2.5}$ with R^2 and root-mean-square error (RMSE) of 0.79 and 0.15 for forests and 0.72 and 0.21 for non-forests, respectively (Fig. 2a and Supplementary Fig. 6a). In forests, leaf area index (LAI) was the most influential predictor, accounting for 12.8% of the spatial variability in $SV_{PM2.5}$. O_3, $PM_{2.5}$, soil water content and nitrogen deposition also showed relatively high explanatory power (Fig. 2b). In non-forests, radiation conditions dominated the spatial pattern of $SV_{PM2.5}$ and explained 15.4% of the variability (Supplementary Fig. 6b). Negative SHAP values were mainly distributed in forests with relatively low LAI and high O_3 (Fig. 2c) and in non-forests with low radiation and high PPT (Supplementary Fig. 6c). Strong interactions were detected mainly among the most influential predictors in forests (Fig. 2d), whereas in non-forests, interaction strengths were more evenly distributed with no dominant pattern (Supplementary Fig. 6d).

Photosynthetic inhibition caused by $PM_{2.5}$ pollution

To disentangle the effects of $PM_{2.5}$ on WUE, we examined the mediatory roles of GPP and ET in the $PM_{2.5}$–WUE relation. We first derived the covariate-induced residuals of GPP (e_{GPP}) and ET (e_{ET}) to remove the effects of covariates (Methods). Satellite-based analyses revealed a predominantly negative correlation between $PM_{2.5}$ and e_{GPP} and a weak negative correlation between $PM_{2.5}$ and e_{ET} (Fig. 3a). Flux-based analyses using site–year combined anomalies supported these divergent relations, with a negative $PM_{2.5}$–e_{GPP} correlation ($r = -0.17$, $P < 0.001$) but a non-significant $PM_{2.5}$–e_{ET} correlation (Fig. 3b). We then applied the PCMCI+ causal detection framework, which conditions on time-lagged dependencies and observed climatic drivers to distinguish causality from a spurious correlation (Supplementary Fig. 7 and Methods). Across global grid cells, 36.1% showed detectable causality from $PM_{2.5}$ to GPP, of which 76.1% were negative (Fig. 3c). To identify potential mediating pathways, we evaluated biogeophysical variables linking $PM_{2.5}$ to e_{GPP}: PAR, the maximum rate of carboxylation (VC_{max}; a proxy of photosynthetic capacity), LAI and nitrogen deposition. After controlling for the effects of covariates, partial correlation analyses indicated negative-dominant relations between $PM_{2.5}$ and PAR, VC_{max} and LAI and a positive-inclined relation between $PM_{2.5}$ and nitrogen deposition (Supplementary Fig. 8). Structural equation modelling confirmed overall the pathways from $PM_{2.5}$ to e_{GPP} via PAR, VC_{max}, LAI and nitrogen deposition. Specifically, $PM_{2.5}$ reduces VC_{max} and PAR, slightly decreases LAI, and marginally increases nitrogen deposition, together leading to lower e_{GPP} (Fig. 3d,e).

Limitations of ecosystem models

We further assessed the effects of $PM_{2.5}$ on WUE_{eco} using 15 ecosystem models driven by identical climatic forcings (Methods). Only two models, CABLE-POP and LPX-Bern, reproduced the predominantly negative

https://doi.org/10.1038/s41558-026-02712-y

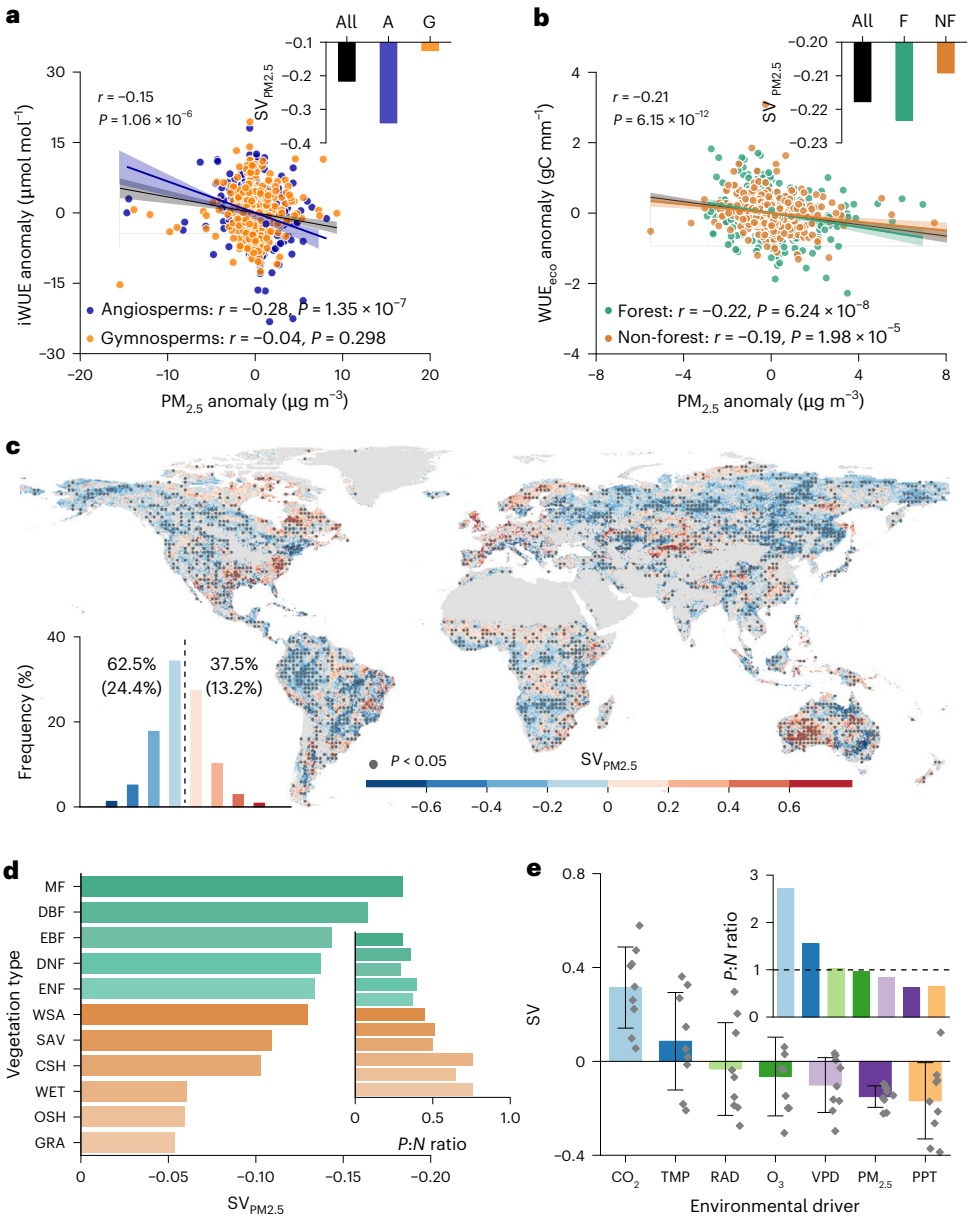

Fig. 1 | Cross-scale relations between $PM_{2.5}$ and plant WUE. a, Relation between site–year combined anomalies of tree-ring iWUE and $PM_{2.5}$ ($n = 1{,}102$). **b**, Relation between site–year combined anomalies of flux-based WUE_{eco} and $PM_{2.5}$ ($n = 1{,}090$). In **a** and **b**, lines show the fits from an ordinary least squares regression, with shading representing the 95% confidence intervals. Insets (**a**,**b**): $SV_{PM2.5}$ derived from a ridge regression that includes CO_2, TMP, PPT, RAD, VPD and O_3 as covariates. **c**, Ensemble mean $SV_{PM2.5}$ of satellite-based WUE_{eco} from nine GPP–ET combinations. Dots indicate grids where the $SV_{PM2.5}$ is significantly different from zero (one-sample *t*-test, $P < 0.05$). **d**, Distribution of spatially averaged $SV_{PM2.5}$ across vegetation types for the satellite-based WUE_{eco} ensemble mean. CSH, closed shrublands; DBF, deciduous broadleaf forests; DNF, deciduous needleleaf forests; EBF, evergreen broadleaf forests; ENF, evergreen needleleaf forests; GRA, grasslands; MF, mixed forests; OSH; open shrublands; SAV, savannahs; WET, wetlands; WSA, woody savannahs. **e**, Comparison of SVs (mean ± s.d.) of a satellite-based WUE_{eco} ensemble ($n = 9$) to environmental drivers. Insets (**d**,**e**): the proportion of grids with positive (*P*) versus negative (*N*) $SV_{PM2.5}$ and SV, respectively. A, angiosperms; F, forests; G, gymnosperms; NF, non-forests. Basemap data in **c** from Natural Earth (https://www.naturalearthdata.com/).

relation between WUE_{eco} and $PM_{2.5}$ observed in satellite-based analyses (Fig. 4a and Supplementary Fig. 9). More than half of the models (8 out of 15) simulated inhibitory effects of $PM_{2.5}$ on GPP, as indicated by the relatively high proportions of grid cells with negative sensitivities (SVs; Fig. 4b). In contrast to observations, which showed a weak negative relation between $PM_{2.5}$ and ET (Fig. 3a), 10 out of 15 models exhibited negative-inclined SVs of ET to $PM_{2.5}$ (Fig. 4c). Overall, the models systematically failed to reproduce the negative $PM_{2.5}$–WUE_{eco} relation found in the observations, with divergent $SV_{PM2.5}$ (observed: −0.17 ± 0.04; modelled: 0.07 ± 0.09, $P < 0.001$) (Fig. 4d). The models also overestimated the effects of CO_2 fertilization, with SVs nearly twice those derived from observations ($P < 0.001$). The relation between e_{GPP} and e_{ET} was stronger in the models ($r = 0.81$, $P < 0.001$) than in the observations ($r = 0.59$, $P = 0.004$) (Fig. 4e).

Discussion

Plant WUE represents a fundamental physiological trait that integrates carbon assimilation and water loss, with broad implications for the capacity of terrestrial ecosystems to mitigate climate change[3,7]. By integrating leaf-level iWUE, ecosystem-scale WUE from eddy-covariance fluxes and satellite-based WUE estimates, we detected predominantly negative correlations between $PM_{2.5}$ and WUE across scales (Fig. 1).

https://doi.org/10.1038/s41558-026-02712-y

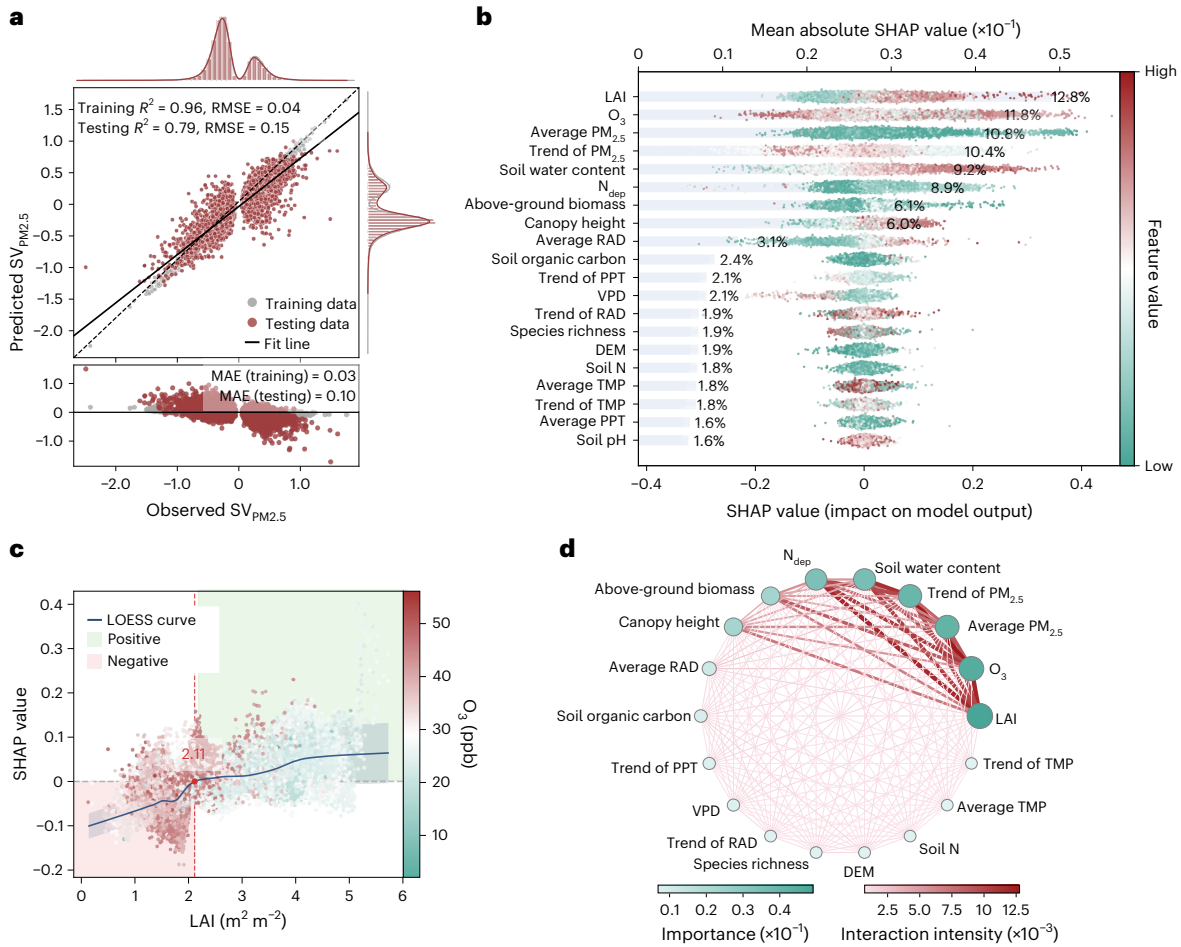

Fig. 2 | Spatial attribution of satellite-based $SV_{PM2.5}$ for forests. a, Evaluation of XGBoost model performance in predicting $SV_{PM2.5}$. **b**, Relative importance of features controlling the spatial variability of $SV_{PM2.5}$, ranked by mean absolute SHAP values. The beeswarm plot shows the distribution of SHAP values for each feature. Variable importance (%) was calculated by normalizing the mean absolute SHAP value of each feature to the sum of the mean absolute SHAP values across all features. DEM (Digital Elevation Model) represents the terrain elevation. **c**, Dependence plots showing how SHAP values vary along the gradients of the two most important features (LAI and O_3). Scatter plot with a LOESS regression curve (blue line) and a shaded blue band representing ±s.d. of the fitted values. **d**, Network of feature interactions based on SHAP interaction values. Node size represents feature importance (consistent with **b**), and edge thickness indicates the strength of pairwise interactions. MAE, mean absolute error; N_{dep}, nitrogen deposition.

Despite methodological and definitional differences among these metrics, together they provide robust evidence that atmospheric particulate pollution weakens carbon–water coupling in terrestrial vegetation. Notably, the inhibitive effect of $PM_{2.5}$ was stronger in forests than in non-forests, and within forests, stronger for angiosperms than for gymnosperms. Broadleaved species typically have thinner leaves and more responsive stomata, making them more vulnerable to light attenuation and stomatal blockage[27]. In addition, dense, multilayered canopies can create microenvironments with longer $PM_{2.5}$ residence times[28], thereby amplifying exposure effects. These results indicate that ecosystems dominated by broadleaved species or dense forests may be disproportionately at risk from air pollution, underscoring the need to incorporate plant trait diversity into ecosystem models.

The spatial heterogeneity of $PM_{2.5}$ effects is shaped by interactions among vegetation traits, pollution levels and climate, resulting in a biome-dependent pattern. In forests, LAI emerged as the dominant control. Forests with high LAI and a complex canopy structure can benefit from enhanced diffuse radiation under light to moderate aerosol loading, which increases photosynthesis in shaded leaves[23,29] and may partly offset the negative effects of $PM_{2.5}$ on WUE (Fig. 2). By contrast, in non-forests with simpler canopy structures, the shading effect of aerosol loading dominates, and regions with low radiation availability tend to exhibit stronger negative $PM_{2.5}$–WUE relations (Supplementary Fig. 6). Also note that $PM_{2.5}$ from different sources can have contrasting effects. Fire-derived aerosols, for example, may alleviate nutrient limitations (for example, nitrogen and phosphorus) through deposition[24,30], thereby potentially boosting carbon assimilation and WUE in nutrient-poor ecosystems. However, $PM_{2.5}$ from urban or industrial areas often contains heavy metals and toxic compounds that impair photosynthesis[25,31]. This source dependence may partly explain the divergent $PM_{2.5}$–WUE relations.

Previous studies have highlighted the asymmetric roles of photosynthesis and stomatal conductance in driving increases in forest WUE, which indicates potential decoupling due to plant acclimation[11,32]. Consistent with this view, we found that $PM_{2.5}$ pollution weakens plant WUE primarily through the inhibition of photosynthesis rather than an alteration of ET (Fig. 3). $PM_{2.5}$-induced declines in VC_{max}, LAI and PAR indicate that several reinforcing mechanisms underlie photosynthetic inhibition. Particulate pollutants can attenuate incoming solar radiation, thereby reducing canopy light availability and altering the diffuse-to-direct radiation ratio in ways that often suppress rather than enhance photosynthesis under heavy pollution[33]. For example, particulate pollution has been linked to weekly cycles of ecosystem productivity in Europe, with reduced photosynthesis on workdays[34], whereas air-quality improvements in China (2013–2017) enhanced spring vegetation productivity by lowering emissions[22]. Direct particle

https://doi.org/10.1038/s41558-026-02712-y

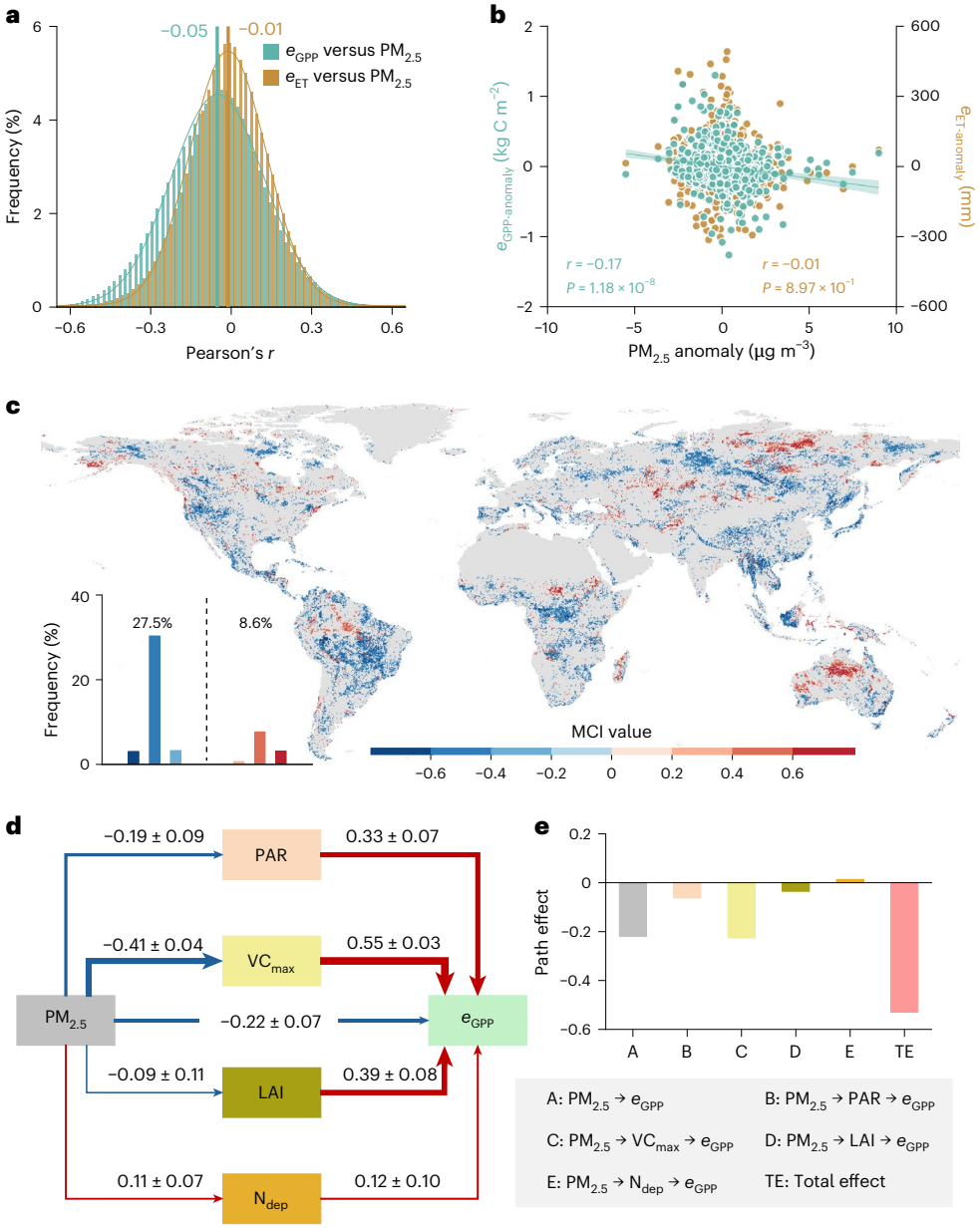

Fig. 3 | Mediatory roles of GPP and ET in the $PM_{2.5}$–WUE relation. a, Relation between $PM_{2.5}$ and covariate-induced residuals of GPP (e_{GPP}) and ET (e_{ET}) (Methods) for satellite-based analyses after removing the effects of covariates. **b**, Relation between $PM_{2.5}$ anomalies and covariate-induced residuals of GPP anomalies ($e_{GPP\text{-}anomaly}$) and ET anomalies ($e_{ET\text{-}anomaly}$) from flux-based analyses. Line shows the fitted values from the ordinary least squares regression, with shading representing the 95% confidence interval. **c**, Causality detection of $PM_{2.5}$ effects on GPP inferred by the PCMCI+ framework (Methods). The momentary conditional independence (MCI) value indicates the strength and direction of the causal link from $PM_{2.5}$ to GPP after conditioning on covariates. **d**, Structural equation model describing pathways from $PM_{2.5}$ to e_{GPP} via PAR, VC_{max}, LAI and nitrogen deposition. Red and blue values indicate positive and negative standardized path coefficients, respectively. Numbers represent means ± 95% confidence intervals from two-sided Wald tests. Arrow widths are proportional to path strengths. **e**, Summary of path effects, including direct, indirect (mediating) and total effect of $PM_{2.5}$ on e_{GPP}. TE, total effect. Basemap data in **c** from Natural Earth (https://www.naturalearthdata.com/).

deposition on leaves can block stomata, reduce mesophyll conductance and induce biochemical stress that downregulates photosynthetic enzymes (such as rubisco) and VC_{max}[22]. Similarly, stronger adverse effects of particulate pollution on photosynthesis have been observed in roadside woody plants under urban conditions, which are associated with reduced efficiency of the photosynthetic apparatus[35]. Declines in LAI under elevated $PM_{2.5}$ may reflect cumulative reductions in canopy growth due to impaired carbon gain[34]. Empirical studies using manipulative experiments or site-level observations have yielded inconsistent results regarding the effects of aerosols on ET due to differences in aerosol composition, plant species and analytical approaches[36,37]. The weak influence of $PM_{2.5}$ on ET observed here probably reflects compensatory effects between reduced photosynthesis and enhanced diffuse radiation, which stabilize canopy water fluxes, whereas hygroscopic aerosols modify the leaf surface microclimate without substantially altering total transpiration rates[38]. Together, these results demonstrate that particulate pollution strongly constrains terrestrial carbon uptake and ecosystem productivity, with limited or uncertain effects on water loss.

A comparison between observations and model simulations revealed that current ecosystem models systematically misrepresent the effects of $PM_{2.5}$ on WUE. Because these models do not use $PM_{2.5}$ or aerosol as a forcing input, they rely solely on vegetation responses

https://doi.org/10.1038/s41558-026-02712-y

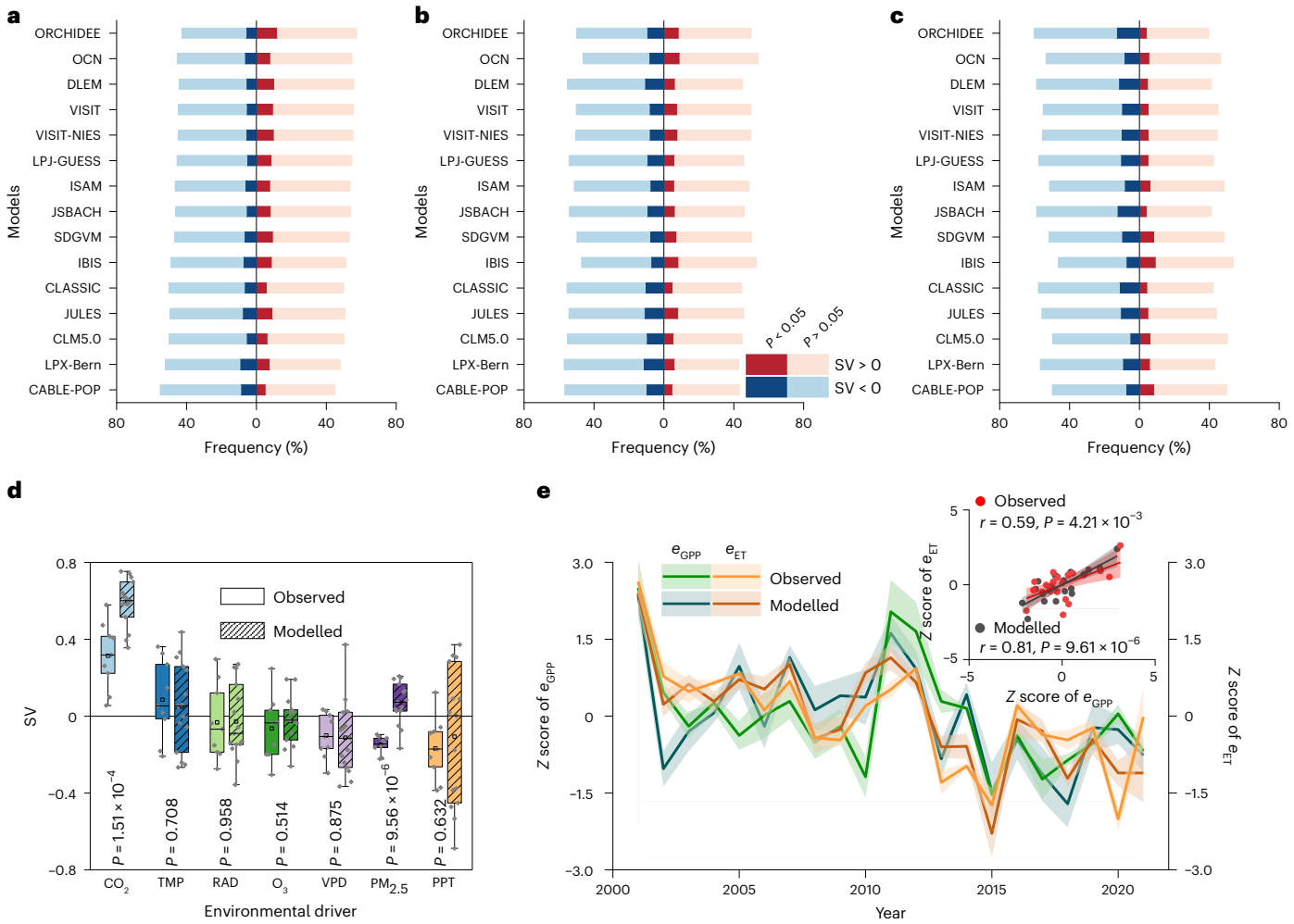

Fig. 4 | Missing representation of $PM_{2.5}$ effects in ecosystem models. **a**–**c**, Frequency of grid cells showing positive versus negative SVs for WUE_{eco} (**a**), GPP (**b**) and ET (**c**) to $PM_{2.5}$ derived from a ridge regression that includes CO_2, climate (TMP, PPT, RAD and VPD), and O_3 as covariates. WUE_{eco}, GPP and ET were derived from 15 ecosystem models (Supplementary Table 3). Significance was determined using two-sided *t*-tests. **d**, Comparison of observed ($n = 9$ ensemble members) and modelled ($n = 15$ models) SVs (mean ± s.d.) of WUE_{eco} to each environmental driver. Box plots display means (open squares), medians (horizontal lines), the 25th and 75th percentiles (box edges), and minimum and maximum values (whiskers). Statistical significance between the two groups was determined using Welch's *t*-test. **e**, *Z* scores of covariate-induced residuals of GPP (e_{GPP}) and ET (e_{ET}) for observations and models (solid lines are means, and the shaded area is ±s.d.). Inset: scatter plot showing the relation between *Z* scores of e_{GPP} and e_{ET}. *r* and *P* values were derived from two-sided *t*-tests.

to covarying climate drivers (CO_2, TMP, PPT, RAD and VPD). The persistent discrepancy between models and observations indicates that these climate-driven responses alone are insufficient to explain the observed effects of $PM_{2.5}$ (Fig. 4). Two key shortcomings are evident. First, although the models captured some degree of photosynthetic inhibition, they largely overestimated $PM_{2.5}$-induced reductions in ET, leading in some cases to neutral or even positive modelled WUE responses. This bias probably reflects the absence of explicit representations of particulate deposition on leaves, stomatal obstruction and boundary layer alterations. Second, models overestimated the effects of CO_2 fertilization on WUE, a long-standing concern in carbon-climate modelling[39,40]. Improving model performance will require a better representation of several key processes, including the partitioning of direct and diffuse radiation and their effects on canopy photosynthesis, dynamic stomatal responses to particle deposition, and the coupling between aerosol deposition and nutrient cycling. Future research should move beyond bulk $PM_{2.5}$ concentration to consider aerosol size distribution and chemical composition. Incorporating these processes into next-generation Earth system models will be essential for improving projections of vegetation–climate feedback under continued air pollution.

Online content

Any methods, additional references, Nature Portfolio reporting summaries, source data, extended data, supplementary information, acknowledgements, peer review information; details of author contributions and competing interests; and statements of data and code availability are available at https://doi.org/10.1038/s41558-026-02712-y.

References

1. Keenan, T. F. et al. Increase in forest water-use efficiency as atmospheric carbon dioxide concentrations rise. *Nature* **499**, 324–327 (2013).
2. Peters, W. et al. Increased water-use efficiency and reduced CO_2 uptake by plants during droughts at a continental scale. *Nat. Geosci.* **11**, 744–748 (2018).
3. Keeling, R. F. et al. Atmospheric evidence for a global secular increase in carbon isotopic discrimination of land photosynthesis. *Proc. Natl Acad. Sci. USA* **114**, 10361–10366 (2017).
4. Huang, M. et al. Change in terrestrial ecosystem water-use efficiency over the last three decades. *Glob. Change Biol.* **21**, 2366–2378 (2015).

5. Drake, B. G., Gonzàlez-Meler, M. A. & Long, S. P. More efficient plants: a consequence of rising atmospheric CO_2? *Annu. Rev. Plant Biol.* **48**, 609–639 (1997).
6. Leakey, A. D. et al. Elevated CO_2 effects on plant carbon, nitrogen, and water relations: six important lessons from FACE. *J. Exp. Bot.* **60**, 2859–2876 (2009).
7. Adams, M. A., Buckley, T. N. & Turnbull, T. L. Diminishing CO_2-driven gains in water-use efficiency of global forests. *Nat. Clim. Change* **10**, 466–471 (2020).
8. Mathias, J. M. & Thomas, R. B. Global tree intrinsic water use efficiency is enhanced by increased atmospheric CO_2 and modulated by climate and plant functional types. *Proc. Natl Acad. Sci. USA* **118**, e2014286118 (2021).
9. Ballantyne, A. P., Alden, C. B., Miller, J. B., Tans, P. P. & White, J. W. C. Increase in observed net carbon dioxide uptake by land and oceans during the past 50 years. *Nature* **488**, 70–72 (2012).
10. Ainsworth, E. A. & Rogers, A. The response of photosynthesis and stomatal conductance to rising CO_2: mechanisms and environmental interactions. *Plant Cell Environ.* **30**, 258–270 (2007).
11. Guerrieri, R. et al. Disentangling the role of photosynthesis and stomatal conductance on rising forest water-use efficiency. *Proc. Natl Acad. Sci. USA* **116**, 16909–16914 (2019).
12. Xu, R. et al. Global population exposure to landscape fire air pollution from 2000 to 2019. *Nature* **621**, 521–529 (2023).
13. Frank, D. C. et al. Water-use efficiency and transpiration across European forests during the Anthropocene. *Nat. Clim. Change* **5**, 579–583 (2015).
14. Adams, M. A., Buckley, T. N., Binkley, D., Neumann, M. & Turnbull, T. L. CO_2, nitrogen deposition and a discontinuous climate response drive water use efficiency in global forests. *Nat. Commun.* **12**, 5194 (2021).
15. Li, F. et al. Global water use efficiency saturation due to increased vapor pressure deficit. *Science* **381**, 672–677 (2023).
16. Brienen, R. J. W. et al. Tree height strongly affects estimates of water-use efficiency responses to climate and CO_2 using isotopes. *Nat. Commun.* **8**, 288 (2017).
17. Querejeta, J. I., Ren, W. & Prieto, I. Vertical decoupling of soil nutrients and water under climate warming reduces plant cumulative nutrient uptake, water-use efficiency and productivity. *New Phytol.* **230**, 1378–1393 (2021).
18. Niu, S. et al. Water-use efficiency in response to climate change: from leaf to ecosystem in a temperate steppe. *Glob. Change Biol.* **17**, 1073–1082 (2011).
19. Li, Y., Wang, Y., Wang, B., Wang, Y. & Yu, W. The response of plant photosynthesis and stomatal conductance to fine particulate matter ($PM_{2.5}$) based on leaf factors analyzing. *J. Plant Biol.* **62**, 120–128 (2019).
20. Wang, B. et al. Elevated aerosol enhances plant water-use efficiency by increasing carbon uptake while reducing water loss. *New Phytol.* **243**, 567–579 (2024).
21. Shim, J., Park, S. & Song, D. Impact of particulate matter (PM_{10}, $PM_{2.5}$) on global horizontal irradiance and direct normal irradiance in urban areas. *Build. Environ.* **271**, 112610 (2025).
22. Qu, W. et al. Delayed leaf green-up is associated with fine particulate air pollution in China. *Nat. Commun.* **16**, 3406 (2025).
23. Strada, S. & Unger, N. Potential sensitivity of photosynthesis and isoprene emission to direct radiative effects of atmospheric aerosol pollution. *Atmos. Chem. Phys.* **16**, 4213–4234 (2016).
24. Descals, A., Janssens, I. A. & Peñuelas, J. Amazon forest nutrient limitation is mitigated by distant fire emissions. *Nat. Geosci.* **19**, 291–295 (2026).
25. Shahid, M. et al. in *Reviews of Environmental Contamination and Toxicology*, Vol. 253 (ed. de Voogt, P.) 65–113 (Springer International Publishing, 2021).
26. Matsumoto, M. et al. Responses of photosynthesis and long-term water use efficiency to ambient air pollution in urban roadside trees. *Urban Ecosyst.* **25**, 1029–1042 (2022).
27. Niinemets, Ü. A review of light interception in plant stands from leaf to canopy in different plant functional types and in species with varying shade tolerance. *Ecol. Res.* **25**, 693–714 (2010).
28. Xu, X. et al. Influence of rainfall duration and intensity on particulate matter removal from plant leaves. *Sci. Total Environ.* **609**, 11–16 (2017).
29. Rap, A. et al. Enhanced global primary production by biogenic aerosol via diffuse radiation fertilization. *Nat. Geosci.* **11**, 640–644 (2018).
30. Mahowald, N. M. et al. Aerosol deposition impacts on land and ocean carbon cycles. *Curr. Clim. Change Rep.* **3**, 16–31 (2017).
31. Hsu, C. Y. et al. Integrated analysis of source-specific risks for $PM_{2.5}$-bound metals in urban, suburban, rural, and industrial areas. *Environ. Pollut.* **275**, 116652 (2021).
32. Zhan, W. et al. Reduced water loss rather than increased photosynthesis controls CO_2-enhanced water-use efficiency. *Nat. Ecol. Evol.* **9**, 1571–1584 (2025).
33. Wang, Z. et al. Aerosol pollution alters the diurnal dynamics of Sun and shade leaf photosynthesis through different mechanisms. *Plant Cell Environ.* **45**, 2943–2953 (2022).
34. He, L. et al. The weekly cycle of photosynthesis in Europe reveals the negative impact of particulate pollution on ecosystem productivity. *Proc. Natl Acad. Sci. USA* **120**, e2306507120 (2023).
35. Popek, R., Przybysz, A., Gawrońska, H., Klamkowski, K. & Gawroński, S. W. Impact of particulate matter accumulation on the photosynthetic apparatus of roadside woody plants growing in the urban conditions. *Ecotoxicol. Environ. Saf.* **163**, 56–62 (2018).
36. Burkhardt, J., Zinsmeister, D., Roth-Nebelsick, A., Hüging, H. & Pariyar, S. Ambient aerosols increase stomatal transpiration and conductance of hydroponic sunflowers by extending the hydraulic system to the leaf surface. *Front. Plant Sci.* **14**, 1275358 (2023).
37. Wang, B. et al. High aerosol loading decreases the transpiration of poplars both in the day-and night-time. *Agric. For. Meteorol.* **327**, 109225 (2022).
38. Burkhardt, J. Hygroscopic particles on leaves: nutrients or desiccants? *Ecol. Monogr.* **80**, 369–399 (2010).
39. Smith Kolby, W. et al. Large divergence of satellite and Earth system model estimates of global terrestrial CO_2 fertilization. *Nat. Clim. Change* **6**, 306–310 (2016).
40. Wang, J. & Liu, D. Models overestimate ecosystem water use efficiency for northern permafrost regions. *Agric. For. Meteorol.* **339**, 109594 (2023).

Methods

Tree-ring-based iWUE data

We compiled tree iWUE data from a global tree-ring $\delta^{13}C$ isotope database spanning 1850–2015, which originally comprised 422 independent isotope series from 134 tree species. Detailed descriptions of data collection, quality control and iWUE calculation methods from isotopic measurements are provided in Adams et al.[7]. For analyses focusing on the period with available $PM_{2.5}$ data (since 2001), we selected 210 sites and excluded those with fewer than 3 years of records. This resulted in a final dataset of 1,102 site–year records from 135 sites representing 73 tree species (Supplementary Fig. 1 and Supplementary Table 1).

Eddy-covariance flux measurements

Eddy-covariance flux data were obtained from FLUXNET2015 and AmeriFlux using annual flux records. All datasets underwent standardized quality control. For sites with records in both FLUXNET2015 and the more recent AmeriFlux database, which provides extended temporal coverage, we prioritized the complete AmeriFlux records rather than merging datasets. To minimize the influence of human activities, all cropland sites were excluded, as were sites with fewer than 3 years of data. The final dataset comprised 1,090 site–year records from 132 sites (Supplementary Fig. 1 and Supplementary Table 2).

Gridded GPP and ET data

We derived monthly GPP data for 2001–2022 from three sources: the Global Land Surface Satellite (GLASS) data[41], the global OCO-2-based Solar-Induced Chlorophyll Fluorescence (SIF) product (GOSIF)[42] and the Penman-Monteith-Leuning model version 2.1.8 (PMLv2)[43]. ET data were obtained from the Simple Terrestrial Hydrosphere model version 2 (SiTHv2)[44], the Global Land Evaporation Amsterdam Model (GLEAM)[45] and the land component of the fifth-generation European ReAnalysis (ERA5L)[46]. Details of these datasets are provided in Supplementary Table 4.

$PM_{2.5}$, ozone, CO_2 and climatic data

Satellite-derived $PM_{2.5}$ data at 1-km spatial resolution were derived from the Global High Air Pollutants dataset, which was generated by integrating big data from satellite aerosol optical depth products, ground-based air-quality measurements, meteorological reanalysis and model outputs[47]. We evaluated the accuracy of the monthly gridded $PM_{2.5}$ dataset for 2001–2022 against ground observations (566,917 site–month records), yielding $R^2 = 0.93$, RMSE = 5.02 μg m^{-3} and mean absolute error of 3.06 μg m^{-3} (Supplementary Fig. 10). For the tree iWUE and flux-based WUE_{eco} analyses, annual $PM_{2.5}$ values were extracted from the gridded data for each site and year. Monthly ozone (O_3) data were also obtained from the Global High Air Pollutants dataset at 10-km resolution. Globally averaged CO_2 concentrations were obtained from the National Oceanic and Atmospheric Administration (NOAA) Global Monitoring Laboratory[48]. For the iWUE and flux-based analyses, we prioritized CO_2 measurements from tree rings and eddy-covariance towers. However, at sites where eddy-covariance-measured CO_2 showed erroneous trends due to calibration issues, NOAA CO_2 data were used to fill or replace missing values. Climatic variables (monthly mean air TMP, mean VPD, accumulated PPT and mean RAD) were obtained from the TerraClimate[49], whereas site-specific flux measurements were used where available.

TRENDY model projections

We analysed GPP and ET outputs (2001–2021) from 15 process-based C cycle models participating in the Trends in the Land Carbon Cycle (TRENDY v.11) project[50]: CABLE-POP, CLASSIC, CLM5.0, DLEM, IBIS, ISAM, JSBACH, JULES, LPJ-GUESS, LPX-Bern, OCN, ORCHIDEE, SDGVM, VISIT and VISIT-NIES (Supplementary Table 3). The TRENDY ensemble simulates ecosystem C dynamics under external forcings, and we focused on outputs from simulation scenario S3, which accounts for temporal changes in land use, climate and atmospheric CO_2 concentrations. This scenario enables an evaluation of the combined impacts of anthropogenic activities and climate change on terrestrial carbon assimilation and water fluxes. Model outputs of GPP and ET were originally produced at monthly time steps and varying spatial resolutions; for consistency, we aggregated them to annual values and regridded all datasets to 0.5° × 0.5° before analysis.

Determination of WUE_{eco} for flux-, satellite- and model-based analyses

For the flux-based analyses, ET was derived from latent heat fluxes, and annual WUE_{eco} was calculated as the ratio of annual GPP to ET at each site. For the satellite-based analysis, we generated an ensemble of WUE_{eco} estimates ($n = 9$; three GPP × three ET datasets). For the model-based analysis, WUE_{eco} was calculated from the GPP and ET outputs of each model. Note that we employed two complementary forms of plant WUE proxies: iWUE and WUE_{eco}. iWUE represents the ratio of carbon assimilation to stomatal conductance at the leaf level, and WUE_{eco} represents the ratio of GPP to ET at the ecosystem level. Although these metrics differ in definition, scale and computation, both capture the coupling between carbon gain and water loss. Their combined use enhances the robustness of our conclusions, as consistent responses across scales provide strong evidence that $PM_{2.5}$ alters plant carbon–water coupling.

Analyses of the relation between $PM_{2.5}$ and plant WUE

Plant WUE is jointly controlled by several environmental factors, so that simple linear correlation or regression analyses may be confounded by combined effects. In this study, we treated the main environmental drivers—CO_2, climate (TMP, PPT, RAD and VPD) and O_3—as covarying drivers (or covariates) of $PM_{2.5}$. To account for potential multicollinearity between $PM_{2.5}$ and the covariates, we applied a ridge regression to estimate environmental SVs. By introducing a penalty term, the ridge regression reduces coefficient variance and yields more robust estimates. All variables were standardized using *Z*-score normalization to ensure the comparability of regression coefficients across drivers.

Given the limited availability of iWUE records for individual sites and species, we pooled all observations to assess the response of iWUE to $PM_{2.5}$. To reduce the influence of background variability, we calculated annual anomalies for iWUE, $PM_{2.5}$ and the covariates by subtracting long-term means from yearly values. Correlation and ridge regression analyses were then used to quantify the relations between iWUE anomalies and $PM_{2.5}$ anomalies. The same approach was applied to flux-based analyses. For the satellite-based analyses, we excluded areas experiencing land-cover change during 2001–2022 using the MODIS product (MCD12Q1.061)[51], and we masked croplands, urban and built-up areas, and barren lands. The ridge regression was then applied to quantify $SV_{PM2.5}$ for each GPP ($n = 3$), ET ($n = 3$) and WUE_{eco} ($n = 9$) dataset.

Beyond the correlation and ridge regression analyses, we used a nonlinear approach, namely generalized additive models, to evaluate the roles of $PM_{2.5}$ and covarying drivers in controlling WUE. With the hierarchical partitioning process, generalized additive models quantify the variance explained by each driver considering both linear and nonlinear responses.

Spatial attribution analysis

We employed explainable machine learning with SHAP to identify the key factors in the spatial distribution of $PM_{2.5}$ effects for forests and non-forests. Predictors included $PM_{2.5}$, O_3, TMP, PPT, RAD, VPD, LAI, plant species richness, canopy height, above-ground biomass, elevation, soil pH, water content, nitrogen and organic carbon. For multi-year $PM_{2.5}$, and climate variables, we calculated both mean values and temporal trends. All predictors are described in Supplementary Table 4. We developed an XGBoost model using these factors as predictors,

with the satellite-based $SV_{PM2.5}$ as the response variable. SHAP values were then computed to interpret the model and quantify the marginal contribution of each predictor. Variable importance was assessed using the mean absolute SHAP values, thereby enabling the ranking of predictors and the identification of the dominant controls on spatial variability in $PM_{2.5}$ effects.

Potential mechanisms underlying the $PM_{2.5}$–WUE relation

We first disentangled the mediating roles of GPP and ET in the $PM_{2.5}$–WUE relation. The ridge regression analyses found a negative-dominant relation between $PM_{2.5}$ and GPP but a neutral relation between $PM_{2.5}$ and ET (Supplementary Fig. 11). We also used covariates (CO_2, climate factors and O_3) to derive residuals of GPP (e_{GPP}) and ET (e_{ET}). We quantified and compared the effects of $PM_{2.5}$ on e_{GPP} and e_{ET} using correlation analyses for both the flux- and satellite-based datasets (Fig. 3a,b). To support causal inference regarding the effects of $PM_{2.5}$ on GPP, we applied the PCMCI+ framework, which combines the Peter–Clark (PC) algorithm with the MCI test and accounts for autocorrelation in time series data[52,53]. This extended framework detects both lagged (time lag $\tau > 0$) and contemporaneous ($\tau = 0$) causal relations. Time series of GPP, $PM_{2.5}$ and the covariates from gridded datasets were used as inputs. A linear partial correlation was adopted as the conditional independence test to emphasize linear dependencies (Supplementary Fig. 7). Model parameters were set as τ_min = 0 and τ_max = 3 to capture dependencies for up to 3 years. Causal strength was quantified using partial correlation values for MCI. Inferred relations are represented as causal graphs (Fig. 3c).

After establishing that $PM_{2.5}$-driven reductions in plant WUE are primarily mediated by photosynthetic inhibition, we conducted pixel-level correlation analyses to examine the intermediary roles of VC_{max}, LAI, SIF, PAR and nitrogen deposition in linking $PM_{2.5}$ to e_{GPP} using the correlation analysis (Supplementary Fig. 8). To further quantify these relations, we applied structural equation modelling to estimate both direct and indirect pathways between $PM_{2.5}$ and e_{GPP}, incorporating PAR, VC_{max}, LAI and nitrogen deposition. All variables were standardized before the analysis, and path coefficients were estimated using maximum likelihood. Path effects were calculated as the product of standardized coefficients along each pathway, and total effects were obtained by summing all associated path effects. Model performance was evaluated using standard fitting criteria: χ^2 test ($P > 0.05$), comparative fit index (>0.9), standardized root-mean-square residual (<0.08), goodness-of-fit index (>0.95) and root-mean-square error of approximation (<0.08). A model was considered acceptable if at least three of these five criteria were satisfied[54].

To assess whether the observed $PM_{2.5}$–WUE relation can be explained solely by vegetation responses to covarying climate drivers, we compared $SV_{PM2.5}$ derived from observations with that simulated by current climate-driven models. The models consistently failed to reproduce the negative $PM_{2.5}$–WUE relation, indicating that real-world $PM_{2.5}$ influences WUE through mechanisms beyond the combined effects of CO_2 and climate. This discrepancy highlights that there are missing processes, such as direct aerosol deposition on leaves, diffuse radiation fertilization, and nitrogen fertilization associated with $PM_{2.5}$, that are not adequately represented in current models.

Data availability

All datasets used in this study are publicly available via open-access repositories. Ground-based $PM_{2.5}$ observations are available via the China National Environmental Monitoring Centre at http://www.cnemc.cn/), the US Environmental Protection Agency (https://www.epa.gov/), the European Air Quality e-Reporting service (https://eeadmz1-downloads-webapp.azurewebsites.net) and the Canadian National Air Pollution Surveillance Program (https://www.canada.ca/en/environment-climate-change/services/air-pollution/monitoring-networks-data/national-air-pollution-program.html). Satellite-based $PM_{2.5}$ and O_3 products are available via the Global High Air Pollutants dataset (https://weijing-rs.github.io/product.html). Gridded GPP data are available via GLASS (https://glass.hku.hk/download.html), GOSIF (https://globalecology.unh.edu/data/GOSIF-GPP.html) and PMLv2 (https://doi.org/10.5281/zenodo.10647618)[55]. Gridded ET data are available via ERA5L (https://doi.org/10.24381/cds.e2161bac), GLEAM (https://www.gleam.eu/) and SiTHv2 (https://doi.org/10.11888/Terre.tpdc.300751). Climatic variables (TMP, PPT, RAD and VPD) were obtained from TerraClimate (https://www.climatologylab.org/terraclimate.html). Global monthly CO_2 records were provided by NOAA (https://gml.noaa.gov/ccgg/trends/global.html). Land-cover type data were obtained from MODIS (https://lpdaac.usgs.gov/products/mcd12c1v061/). LAI data were obtained from MODIS (https://www.earthdata.nasa.gov/data/catalog/lpcloud-mod15a2h-061). PAR data are available via BESS (https://doi.org/10.1111/nph.15703). VC_{max} is available from NESDC (http://www.nesdc.org.cn/). Soil variables (soil organic carbon, soil nitrogen, soil water content and soil pH) are available via SoilGrids (https://www.isric.org/explore/soilgrids). A description of each dataset can be found in Supplementary Table 4. Source data are provided with this paper.

Code availability

The code is available via Zenodo at https://doi.org/10.5281/zenodo.19587583 (ref. 56).

References

41. Liang, S. et al. The global land surface satellite (GLASS) product suite. *Bull. Am. Meteorol. Soc.* **102**, 323–337 (2021).
42. Li, X. & Xiao, J. Mapping photosynthesis solely from solar-induced chlorophyll fluorescence: a global, fine-resolution dataset of gross primary production derived from OCO-2. *Remote Sens.* **11**, 2563 (2019).
43. Zhang, Y. et al. Coupled estimation of 500 m and 8-day resolution global evapotranspiration and gross primary production in 2002–2017. *Remote Sens. Environ.* **222**, 165–182 (2019).
44. Zhang, K. et al. A global dataset of terrestrial evapotranspiration and soil moisture dynamics from 1982 to 2020. *Sci. Data* **11**, 445 (2024).
45. Miralles, D. G. et al. GLEAM4: global land evaporation and soil moisture dataset at 0.1 resolution from 1980 to near present. *Sci. Data* **12**, 416 (2025).
46. Muñoz-Sabater, J. et al. ERA5-Land: a state-of-the-art global reanalysis dataset for land applications. *Earth Syst. Sci. Data* **13**, 4349–4383 (2021).
47. Wei, J. et al. First close insight into global daily gapless 1 km $PM_{2.5}$ pollution, variability, and health impact. *Nat. Commun.* **14**, 8349 (2023).
48. Lan, X., Tans, P. & Thoning, K. *Trends in Globally-averaged CO_2 Determined from NOAA Global Monitoring Laboratory Measurements* Report (NOAA GML, 2023); https://doi.org/10.15138/9n0h-zh07.
49. Abatzoglou, J. T., Dobrowski, S. Z., Parks, S. A. & Hegewisch, K. C. TerraClimate, a high-resolution global dataset of monthly climate and climatic water balance from 1958–2015. *Sci. Data* **5**, 170191 (2018).
50. Friedlingstein, P. et al. Global carbon budget 2022. *Earth Syst. Sci. Data* **14**, 4811–4900 (2022).
51. Friedl, M. & Sulla-Menashe, D. *MODIS/Terra+Aqua Land Cover Type Yearly L3 Global 500 m SIN Grid V061* Report (NASA Land Processes Distributed Active Archive Center, 2022); https://doi.org/10.5067/MODIS/MCD12Q1.061
52. Spirtes, P. & Glymour, C. An algorithm for fast recovery of sparse causal graphs. *Soc. Sci. Comput. Rev.* **9**, 62–72 (1991).
53. Runge, J. et al. Inferring causation from time series in Earth system sciences. *Nat. Commun.* **10**, 2553 (2019).

54. Gao, S. et al. An earlier start of the thermal growing season enhances tree growth in cold humid areas but not in dry areas. *Nat. Ecol. Evol.* **6**, 397–404 (2022).
55. Zhang, Y., Kong, D. & Xu, Z. PML_V2.1.8 global evapotranspiration and gross primary production (2000.02-2023.12) [Deprecated]. *Zenodo* https://doi.org/10.5281/zenodo.10647618 (2024).
56. Wang, J. Particulate air pollution undermines plant water-use efficiency by inhibiting photosynthesis. *Zenodo* https://doi.org/10.5281/zenodo.19587583 (2026).

Acknowledgements

We thank S. Sitch and M. O'Sullivan for sharing the TRENDY data. We also thank the principal investigators of all publicly available datasets used in this study for making their valuable data available.

Author contributions

Y.Z. and C.W. designed this study. J. Wang performed the analyses and visualization and wrote the first draft of the paper. J. Wei produced the air pollution data. Y.Z., L.L. and C.M.Z. discussed the results and contributed to the revisions.

Funding

This study was supported by the National Natural Science Foundation of China (Grant No. 42125101), the University of Hong Kong HKU-100 Scholars Fund, Research Grants Council—Strategic Topics Grant (Grant No. STG2/P-705/24-R) and the HKU Social Sciences Internal Seed Grant Scheme. J. Wang was funded by the National Natural Science Foundation of China (Grant No.42571037) and the Kezhen and Bingwei Young Scientist Program of IGSNRR. C.M.Z was supported by a European Research Council (ERC) Consolidator Grant under the European Union's Horizon Europe research and innovation programme (grant agreement No. 101229851, CHILL-TIME).

Competing interests

The authors declare no competing interests.

Additional information

Supplementary information The online version contains supplementary material available at https://doi.org/10.1038/s41558-026-02712-y.

Correspondence and requests for materials should be addressed to Yuyu Zhou or Chaoyang Wu.

Peer review information *Nature Climate Change* thanks the anonymous reviewers for their contribution to the peer review of this work.